

Isoscalar giant monopole resonance in ^{24}Mg and ^{28}Si : Effect of coupling between the isoscalar monopole and quadrupole strength

A. Bahini,^{1,2,*} V. O. Nesterenko,^{3,4,5,†} I. T. Usman,¹ P. von Neumann-Cosel,⁶ R. Neveling,² J. Carter,¹ J. Kvasil,⁷ A. Repko,^{7,8} P. Adsley,^{1,2,9,10} N. Botha,¹ J. W. Brummer,^{2,9} L. M. Donaldson,² S. Jongile,^{2,9} T. C. Khumalo,^{1,2,11} M. B. Latif,^{1,2} K. C. W. Li,^{2,9} P. Z. Mabika,¹² P. T. Molema,^{1,2} C. S. Moodley,^{1,2} S. D. Olorunfunmi,^{1,2} P. Papka,^{2,9} L. Pellegrini,^{1,2} B. Rebeiro,¹² E. Sideras-Haddad,¹ F. D. Smit,² S. Triambak,¹² and J. J. van Zyl⁹

¹*School of Physics, University of the Witwatersrand, Johannesburg 2050, South Africa*

²*iThemba Laboratory for Accelerator Based Sciences, Somerset West 7129, South Africa*

³*Laboratory of Theoretical Physics, Joint Institute for Nuclear Research, Dubna, Moscow Region 141980, Russia*

⁴*State University "Dubna", Dubna, Moscow Region 141980, Russia*

⁵*Moscow Institute of Physics and Technology, Dolgoprudny, Moscow Region 141701, Russia*

⁶*Institut für Kernphysik, Technische Universität Darmstadt, D-64289 Darmstadt, Germany*

⁷*Institute of Particle and Nuclear Physics, Charles University, CZ-18000, Prague 8, Czech Republic*

⁸*Institute of Physics, Slovak Academy of Sciences, 84511, Bratislava, Slovakia*

⁹*Department of Physics, Stellenbosch University, 7602 Matieland, Stellenbosch, South Africa*

¹⁰*Irene Joliot Curie Lab, UMR8608, IN2P3-CNRS, Université Paris Sud 11, 91406 Orsay, France*

¹¹*Department of Physics, University of Zululand, Richards Bay, 3900, South Africa*

¹²*Department of Physics and Astronomy, University of the Western Cape, Bellville 7535, South Africa*

(Dated: November 16, 2021)

Background: In highly deformed nuclei, there is a noticeable coupling of the Isoscalar Giant Monopole Resonance (ISGMR) and the $K = 0$ component of the Isoscalar Giant Quadrupole Resonance (ISGQR), which results in a double peak structure of the isoscalar monopole (IS0) strength (a narrow low-energy deformation-induced peak and a main broad ISGMR part). The energy of the narrow low-lying IS0 peak is sensitive to both the incompressibility modulus K_∞ and the coupling between IS0 and isoscalar quadrupole (IS2) strength.

Objective: This study aims to investigate the two-peaked structure of the ISGMR in the prolate ^{24}Mg and oblate ^{28}Si nuclei and identify among a variety of energy density functionals based on Skyrme parameterisations the one which best describes the experimental data. This will allow for conclusions regarding the nuclear incompressibility. Because of the strong IS0/IS2 coupling, the deformation splitting of the ISGQR will also be analysed.

Methods: The ISGMR was excited in ^{24}Mg and ^{28}Si using α -particle inelastic scattering measurements acquired with an $E_\alpha = 196$ MeV beam at scattering angles $\theta_{\text{Lab}} = 0^\circ$ and 4° . The K600 magnetic spectrometer at iThemba LABS was used to detect and momentum analyse the inelastically scattered α particles. An experimental energy resolution of ≈ 70 keV (FWHM) was attained, revealing fine structure in the excitation-energy region of the ISGMR. The IS0 strength distributions in the nuclei studied were obtained with the Difference-of-Spectrum (DoS) technique. The theoretical comparison is based on the quasiparticle random-phase approximation (QRPA) with a representative set of Skyrme forces.

Results: IS0 strength distributions for ^{24}Mg and ^{28}Si are extracted and compared to previously published results from experiments with a lower energy resolution. With some exceptions, a reasonable agreement is obtained. The IS0 strength is found to be separated into a narrow structure at about 13 – 14 MeV in ^{24}Mg , 17 – 19 MeV in ^{28}Si and a broad structure at 19 – 26 MeV in both nuclei. The data are compared with QRPA results. The results of the calculated characteristics of IS0 states demonstrate the strong IS0/IS2 coupling in strongly prolate ^{24}Mg and oblate ^{28}Si . The narrow IS0 peaks are shown to arise due to the deformation-induced IS0/IS2 coupling and strong collective effects. The cluster features of the narrow IS0 peak at 13.87 MeV in ^{24}Mg are also discussed. The best description of the IS0 data is obtained using the Skyrme force SkP^o with an associated low nuclear incompressibility $K_\infty = 202$ MeV allowing for both the energy of the peak and integral IS0 strength in ^{24}Mg and ^{28}Si to be reproduced. The features of the ISGQR in these nuclei are also investigated. An anomalous deformation splitting of the ISGQR in oblate ^{28}Si is found.

Conclusions: The ISGMR and ISGQR in light deformed nuclei are coupled and thus need to be described simultaneously. Only such a description is relevant and consistent. The deformation-induced narrow IS0 peaks can serve as an additional sensitive measure of the nuclear incompressibility.

*armand.bahini@wits.ac.za

†nester@theor.jinr.ru

I. INTRODUCTION

For many years, the Isoscalar Giant Monopole Resonance (ISGMR) served as an important source of information on the nuclear incompressibility [1–3]. In deformed nuclei, this resonance demonstrates a remarkable coupling of the isoscalar monopole and quadrupole ($K = 0$) modes, which leads to a double peak structure of the IS0 strength [4–10] (here, K stands for the projection of the total angular momentum on the symmetry axis of an axially deformed nucleus [11]). Strongly deformed light nuclei, like prolate ^{24}Mg and oblate ^{28}Si , are especially attractive for an exploration of the nuclear incompressibility K_∞ and the role of the IS0/IS2 coupling. Indeed, in these nuclei, one may expect a deformation-induced strong narrow peak in the IS0 strength located below the main ISGMR region [12–14]. The energy of this peak should be sensitive to both the incompressibility K_∞ and the IS0/IS2 coupling strength.

The ISGMR in ^{24}Mg has been explored in (α, α') and $(^6\text{Li}, ^6\text{Li}')$ experiments since the 1980s (see Ref. [2] for the extensive review and discussion). More recent (α, α') experiments were performed at the Research Center for Nuclear Physics (RCNP) for ^{24}Mg [12, 14, 15] and ^{28}Si [16]. In 2021, the results of an RCNP $(^6\text{Li}, ^6\text{Li}')$ experiment on IS0 strength in ^{24}Mg were published [17]. The IS0/IS2 coupling was mentioned in Refs. [12, 17] in order to explain the existence of the IS0 structure located around 16 – 19 MeV excitation in ^{24}Mg . The existence of a prominent IS0 peak at about 18 MeV in oblate ^{28}Si was noted but not yet explained [16]. These results generally confirm previous findings from (α, α') experiments performed by the Texas A&M University (TAMU) group on ^{24}Mg [18] (for the dataset where the out-of-plane angle was measured) and ^{28}Si [19]. For ^{28}Si , discrepancies between RCNP [16] and TAMU [19] results in the high excitation-energy region above 20 MeV were noted and attributed to the phenomenological background subtraction method employed by TAMU [3].

The IS0/IS2 coupling was earlier considered within the quasiparticle random phase approximation (QRPA) in ^{24}Mg [12–14, 17, 20, 21] and ^{28}Si [21]. However, in the study [21], the narrow IS0 peaks in ^{24}Mg and ^{28}Si were not specifically discussed. Furthermore, one can dispute whether the low-energy narrow IS0 peak in ^{24}Mg has been correctly assigned (and used in the QRPA analysis) in the RCNP studies [12, 14, 17] (see discussion in Sect. IVB).

In this paper, the ISGMR in prolate ^{24}Mg and oblate ^{28}Si is explored using α -particle inelastic scattering measurements with an $E_\alpha = 196$ MeV beam measured at scattering angles $\theta_{\text{Lab}} = 0^\circ$ and 4° using the high energy-resolution K600 magnetic spectrometer at the iThemba Laboratory for Accelerator Based Science (LABS), South Africa. The study focuses on the deformation-induced splitting of the ISGMR into two parts: a narrow peak arising due to IS0/IS2 coupling, and a wide structure representing the main ISGMR. The former exists only in

deformed nuclei while the latter appears in both spherical and deformed nuclei.

By comparing the experimental data obtained with QRPA calculations, we will identify the narrow IS0 peak in ^{24}Mg , explain the origin of the narrow IS0 peaks in both prolate ^{24}Mg and oblate ^{28}Si , and suggest a Skyrme force suitable for the description of IS0 strength in these nuclei. Moreover, we will analyse in detail the IS2 strength, which determines the energy of the narrow IS0 peak, and show that, in strongly deformed nuclei, only a simultaneous description of IS0 and IS2 strengths can be considered as consistent. The simultaneous availability of data for a prolate (^{24}Mg) and an oblate (^{28}Si) case allows for the generalisation of the conclusions.

The paper is organised as follows: in Sec. II, the experimental details are given. The method of extraction and the resulting IS0 strength distributions are presented in Sec. III while, in Sec. IV, details of the QRPA calculations are given and the comparison with the data is shown and discussed. In Sec. V, conclusions are drawn and finally in Appendix A, the predicted deformation splitting of the ISGQR in ^{24}Mg and ^{28}Si is presented.

II. EXPERIMENTAL DETAILS

The experimental procedure followed in this study is similar to that described elsewhere [21, 22]. As such, only salient details are provided here. The experiment was performed at the Separated Sector Cyclotron (SSC) facility of iThemba LABS using a beam of 196 MeV α particles. Inelastically scattered α particles were momentum analysed by the K600 magnetic spectrometer after interacting with either a 0.23 mg/cm² thick ^{24}Mg or a 0.23 mg/cm² thick ^{28}Si foil. The horizontal and vertical positions of the scattered α particles in the focal plane of the spectrometer were measured using two multiwire drift chambers. Energy deposition in plastic scintillators in the focal plane as well as time-of-flight measurements relative to the cyclotron radio frequency were used for particle identification.

Spectra were acquired with the spectrometer set at scattering angles 0° and 4° . In the former, scattering angles $\theta_{\text{Lab}} = 0^\circ \pm 1.91^\circ$ and in the latter, scattering angles from $\theta_{\text{Lab}} = 2^\circ$ to 6° were covered by a circular spectrometer aperture, respectively. The trajectory of the scattered particles through the focal plane was used to construct the scattering angle. A multihole collimator was used to calibrate the measured focal-plane angles to scattering trajectories into the spectrometer.

In the zero-degree mode, both the unscattered beam and the inelastically scattered particles are transported through the K600 magnetic spectrometer with the beam exiting the spectrometer only a few centimeters away from the drift chamber position in the high-dispersion focal plane mode of the K600. For such measurements, suppression of beam-induced background is critical. In order to subtract the instrumental background, a standard

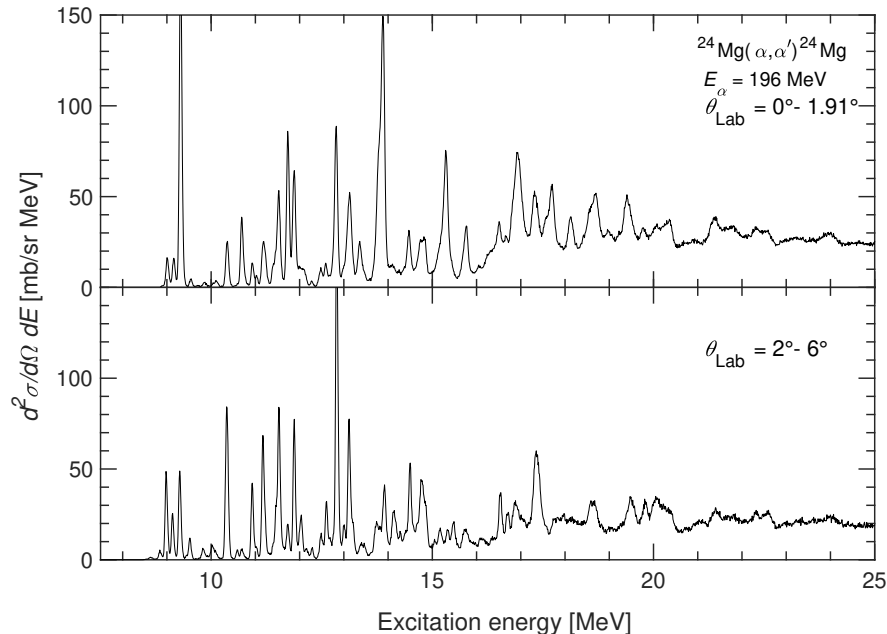


FIG. 1: Double-differential cross sections for the $^{24}\text{Mg}(\alpha, \alpha')$ reaction at $E_\alpha = 196$ MeV with $\theta_{\text{Lab}} = 0^\circ - 1.91^\circ$ (top) and $\theta_{\text{Lab}} = 2^\circ - 6^\circ$ (bottom).

method used at the iThemba LABS K600 [23] and the RCNP magnetic spectrometers [24] that exploits differences in the vertical distribution of real and background events was employed. This method establishes background spectra from the regions of the focal plane above and below the vertically focussed band of true events and allows a direct subtraction of these components from the central region of interest. In contrast to the zero-degree mode, improved instrumental background conditions in the small-angle mode allows one to operate the spectrometer in vertical off-focus mode and also use the medium-dispersion focal plane. In the off-focus mode, the vertical position on the focal plane relates to the vertical component of the scattering angle into the spectrometer aperture and allows for its reconstruction [24].

The same techniques as employed in Ref. [22] were adopted for the analysis of the data. This includes software corrections of kinematic effects and optical aberrations in the horizontal focal-plane position that depend on the vertical focal-plane position and the scattering angle into the spectrometer. The energy calibration was based on well-known states in ^{24}Mg [15, 25]. An energy resolution of ≈ 70 keV (FWHM) was attained. Figures 1 and 2 show the inelastic scattering cross sections extracted at $0^\circ - 1.91^\circ$ and $2^\circ - 6^\circ$ for ^{24}Mg and ^{28}Si , respectively. The broad structure seen in Fig. 2 below 10 MeV is due to hydrogen contaminants in the targets. However, it does not affect the excitation-energy ranges relevant for the extraction of the ISO strength as demonstrated in the next section.

III. EXPERIMENTAL RESULTS

The Multipole Decomposition Analysis (MDA) technique was employed in numerous studies to extract the ISO strength distribution in nuclei [3, 12, 14, 16–19, 26, 27]. However, due to the limited number of angular data points in the present study, the ISO strength distributions were rather determined via the Difference-of-Spectra (DoS) method [28]. In the DoS method, an excitation-energy spectrum for the angular region associated with the first minimum of the $L = 0$ angular distribution is subtracted from the excitation-energy spectrum taken at 0° . This method, therefore, requires the determination of the suitable angle cut from the measurement at $\theta_{\text{Lab}} = 2^\circ - 6^\circ$, which is obtained from DWBA calculations.

In the present study, the DWBA calculations were performed according to the method described in Ref. [29]. A density-dependent single-folding model for the real part of the potential $U(r)$, obtained with a Gaussian α -nucleon potential, and a phenomenological Woods-Saxon potential for the imaginary term of $U(r)$ were used, so that the α -nucleus potential can be written as

$$U(r) = V_{\text{fold}}(r) + i \frac{W}{\{1 + \exp[(r - R_1)/a_1]\}}, \quad (1)$$

with radius $R_1 = r_{01}(A_p^{1/3} + A_t^{1/3})$ and diffuseness a_1 . The subscripts p and t refer to projectile and target, respectively, and A denotes the mass number. The potential $V_{\text{fold}}(r)$ is obtained by folding the ground-state density

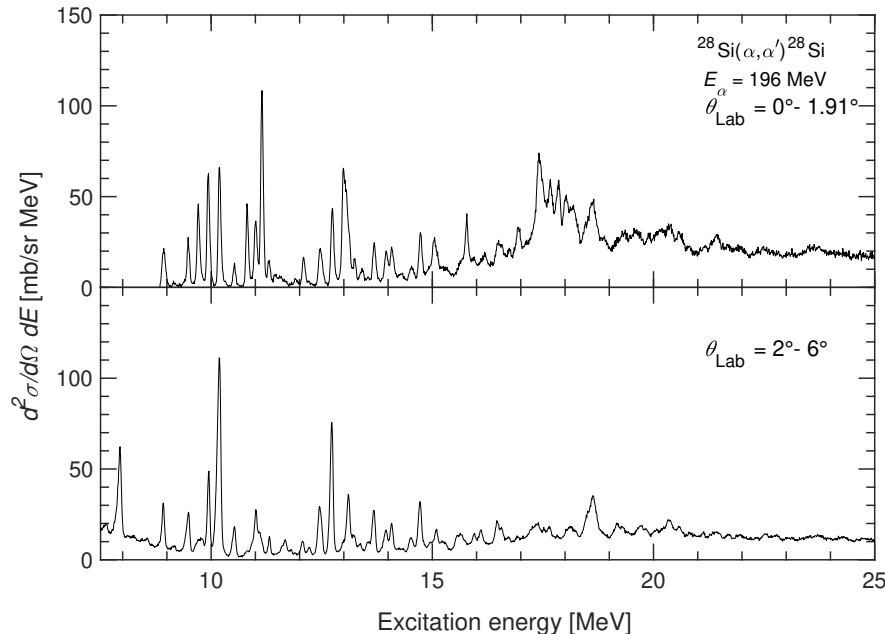


FIG. 2: Same as Fig. 1, but for ^{28}Si .

with a density-dependent α -nucleon interaction

$$V_{\text{fold}}(r) = -V \int d^3 r' \rho(r') \left[1 - \beta \rho(r')^{2/3} \right] \exp(-z^2/t^2), \quad (2)$$

where $z = |r - r'|$ is the distance between the centre of mass of the α particle and a target nucleon, and $\rho(r')$ is the ground-state density of the target nucleus at the position r' of the target nucleon. The parameters $\beta = 1.9 \text{ fm}^2$ and range $t = 1.88 \text{ fm}$ were taken from Ref. [29]. The ground-state density $\rho(r)$ of the target nucleus at the position r is given by

$$\rho(r) = \frac{\rho_0}{1 + \exp\left(\frac{r-c}{a}\right)}, \quad (3)$$

where the Fermi-distribution parameters c and a describe the half-density radius and the diffuseness, respectively. Numerical values for ^{24}Mg and ^{28}Si were taken from Ref. [30].

DWBA calculations were carried out using the computer code PTOLEMY [31, 32]. The Optical Model Parameters (OMP) used in the DWBA calculations, viz. r_{0I} , a_I , V and W , for each nucleus are usually obtained by fitting elastic scattering cross sections. The procedure is fully described in Ref. [33]. However, due to the lack of elastic scattering data in this study, the parameters were taken from studies of the TAMU group on the same nuclei. This is justified by the similarity of their beam energy (240 MeV) compared to this study. The OMP parameters are summarised in Table I.

TABLE I: Optical model parameters taken from the TAMU group publications.

Nucleus	V (MeV)	W (MeV)	r_{0I} (fm)	a_I (fm)	Refs.
^{24}Mg	41.02	35.39	0.934	0.614	[34]
^{28}Si	44	32.5	0.9306	0.687	[35]

The measured cross sections can be converted to fractions of the EWSR (a_0) by comparing with DWBA calculations assuming 100% EWSR, which are shown in Fig. 3. The strength is then calculated using the a_0 values and is expressed as

$$S_0(E_x) = \frac{2\hbar^2 A \langle r^2 \rangle}{m E_x} a_0(E_x), \quad (4)$$

where m is the nucleon mass, E_x is the excitation energy corresponding to a given state or energy bin, and $\langle r^2 \rangle$ is the second moment of the ground-state density. We use $\langle r^2 \rangle = 9.945 \text{ fm}^2$ for ^{24}Mg and 9.753 fm^2 for ^{28}Si .

The DoS technique relies on the subtraction of the contributions of all multipoles except $L = 0$ from the 0° spectrum using data from an angle range defined by the first minimum of the $L = 0$ contribution. It was shown that the sum of angular distributions of all multipoles $L > 0$ is similar at the maximum and first minimum of the $L = 0$ distribution [3, 28]. Hence, the subtraction of the inelastic spectrum associated with the flat angular distribution (where $L = 0$ is at a minimum from the

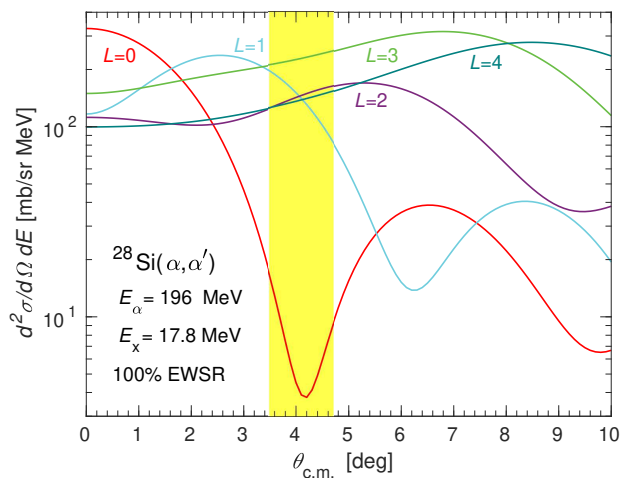
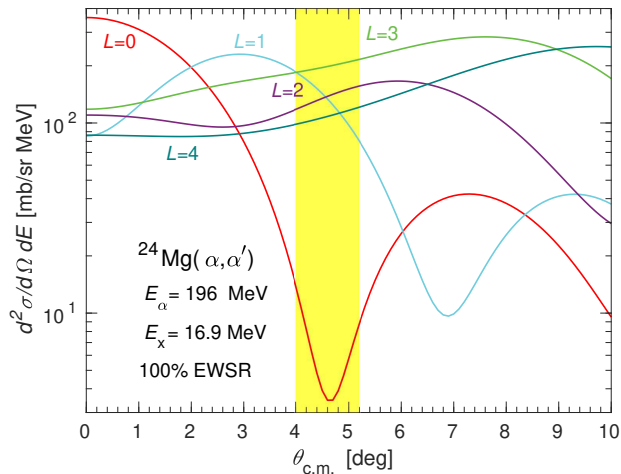


FIG. 3: DWBA calculations of the differential cross sections for the $^{24}\text{Mg}(\alpha, \alpha')$ (top panel) and $^{28}\text{Si}(\alpha, \alpha')$ (bottom panel) reaction at $E_\alpha = 196$ MeV for various isoscalar electric multipoles. The calculations have been normalised to 100% of the appropriate EWSR at an excitation energy of 16.9 MeV in ^{24}Mg and 17.8 MeV in ^{28}Si .

0° spectrum) is assumed to represent essentially the ISO component excited in α -inelastic scattering close to 0° .

The direct subtraction of the angle cut spectrum from the spectrum at $0^\circ \leq \theta_{\text{Lab}} \leq 1.91^\circ$ (blue) yields the black difference spectra shown in the upper and lower panels of Fig. 4 for ^{24}Mg and ^{28}Si , respectively. The angle cut for each nucleus is indicated by the highlighted yellow area in Fig. 3 and listed in Table II. The angle corresponding to the minimum of the $L = 0$ distribution is also indicated.

ISO strength distributions in ^{24}Mg and ^{28}Si were determined from the difference spectra. The fraction of ISO strength in EWSR per MeV was obtained by dividing the extracted experimental ISO component by the corresponding integral value of $L = 0$, 100% EWSR obtained at the average angles $\theta_{\text{c.m.}}^{\text{av.}} = 1.13^\circ$ (^{24}Mg) and 1.12° (^{28}Si) in the 0° spectra. The results are shown in

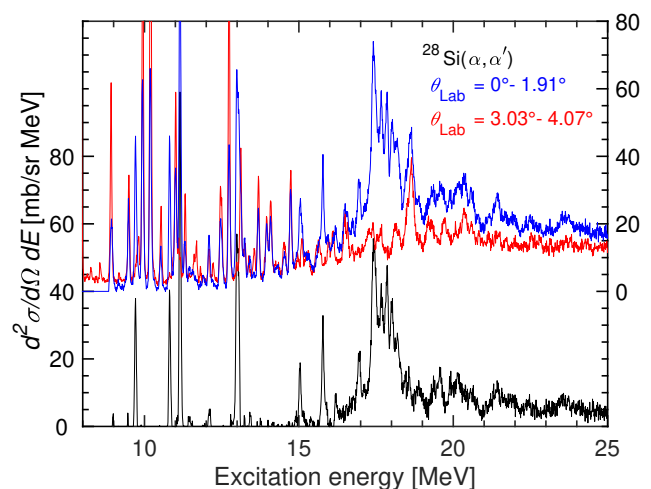
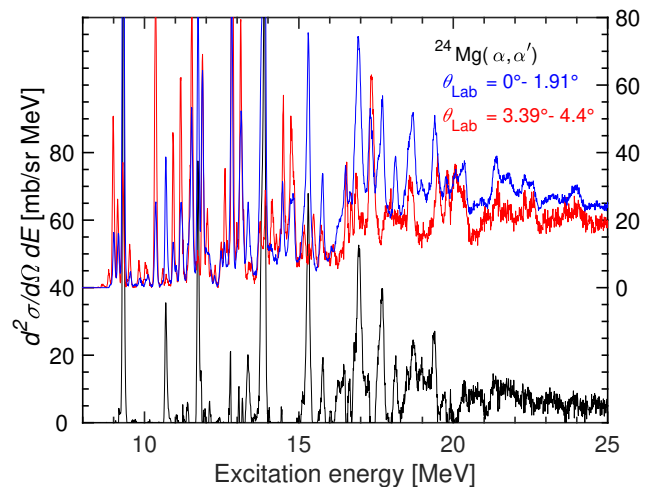


FIG. 4: Double-differential cross sections for $^{24}\text{Mg}(\alpha, \alpha')$ (top panel) and $^{28}\text{Si}(\alpha, \alpha')$ (bottom panel) at $E_\alpha = 196$ MeV. The blue and red spectra represent the data acquired at $0^\circ \leq \theta_{\text{Lab}} \leq 1.91^\circ$ and at $3.39^\circ \leq \theta_{\text{Lab}} \leq 4.4^\circ$ for ^{24}Mg and $3.03^\circ \leq \theta_{\text{Lab}} \leq 4.07^\circ$ for ^{28}Si , respectively. For clarity, these spectra are shifted by 40 mb/sr MeV. The black spectra represent the difference calculated using the DoS technique (see text).

TABLE II: Angle cuts implemented in the 4° dataset to define the angular region around the first $L = 0$ minimum.

Nucleus	^{24}Mg	^{28}Si
Angle cut (θ_{Lab})	$3.39^\circ - 4.4^\circ$	$3.03^\circ - 4.07^\circ$
Angle cut ($\theta_{\text{c.m.}}$)	$4^\circ - 5.2^\circ$	$3.5^\circ - 4.7^\circ$
$L = 0$ minimum ($\theta_{\text{c.m.}}$)	4.6°	4.1°

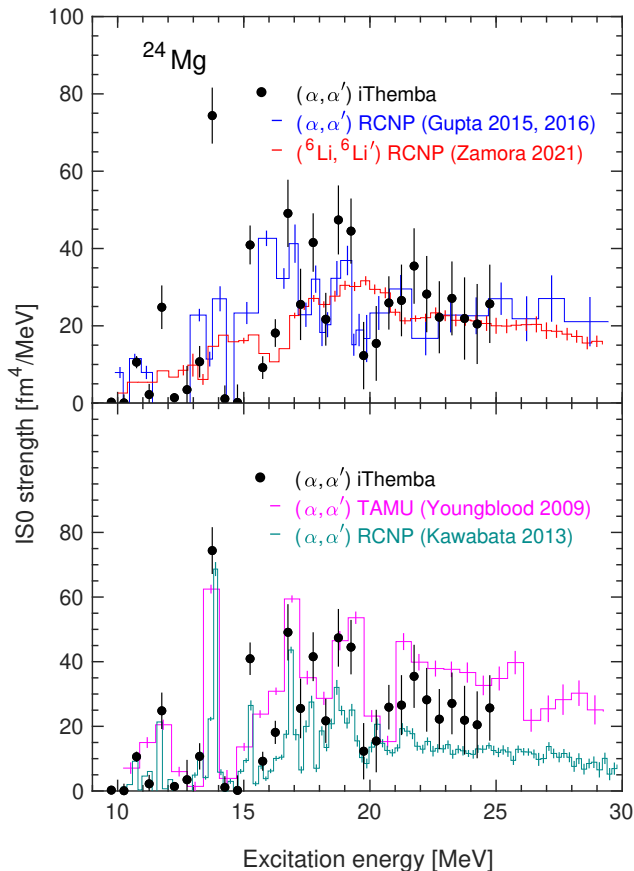


FIG. 5: IS0 strength distributions in ^{24}Mg . The present iThemba LABS data are shown as black filled circles. Also shown are the (α, α') [12, 14] and $({}^6\text{Li}, {}^6\text{Li}')$ data [17] from the RCNP shown as blue and red histograms, respectively (top panel). The bottom panel displays results from TAMU [18] (magenta histogram) and a different measurement at RCNP [15] shown by dark cyan histogram.

Figs. 5 and 6 for 0.5 MeV wide energy bins. The uncertainties shown include both systematical and statistical errors. For comparison purposes, the IS0 strengths from the RCNP experiments ([12, 14, 15] for ^{24}Mg and [16] for ^{28}Si) and the TAMU experiments ([18] for ^{24}Mg and [19] for ^{28}Si) are also shown. The results from Ref. [18] are for the dataset where the out-of-plane angle was measured. For better visibility the comparison of IS0 strength distributions with the present results in Fig. 5 for ^{24}Mg is split into two parts. The upper part shows results from Refs. [12, 14], [17] and the lower those from Refs. [15] and [18].

Data for ^{24}Mg from the present study generally agree within error bars with the RCNP and TAMU data. However, above 17 MeV the IS0 strength from the TAMU group is consistently higher than both the iThemba LABS and RCNP strengths. These discrepancies might

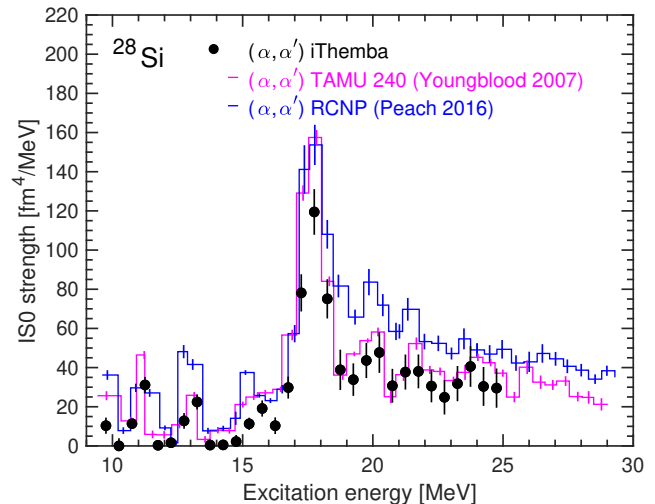


FIG. 6: IS0 strength distribution in ^{28}Si . The present iThemba data are shown as black filled circles. Data shown as blue and magenta histograms with vertical error bars are from RCNP [16] and TAMU [19].

be attributed to the background-subtraction method employed by the TAMU group. At the same time, Fig. 5 shows that the RCNP [12, 14], TAMU [18] and present iThemba LABS data for ^{24}Mg give somewhat different strength distributions below the main ISGMR region. In particular, the RCNP experiments [12, 14] suggest the highest IS0 structures at 16 – 20 MeV and a two times lower peak at 13 – 16 MeV. A similar structure was observed in the recent $({}^6\text{Li}, {}^6\text{Li}')$ experiment [17]. Instead, the TAMU and iThemba LABS data (bottom panel of Fig. 5) give the highest IS0 peak at about 13.8 MeV and a broader peak with a maximum at about 18 MeV. It is remarkable that, unlike the RCNP data [12, 14], another (α, α') experiment at RCNP with superior energy resolution [15] does show the strong narrow peak at 13.8 MeV (bottom panel of Fig. 5). Moreover, this peak was clearly observed in the early (α, α') [36] and $({}^6\text{Li}, {}^6\text{Li}')$ [37] experiments (see the discussion in Sec. 4.2.3 of Ref. [2]). So most of the experimental datasets confirm the existence of the strong narrow IS0 peak at 13.8 – 13.9 MeV in ^{24}Mg . As can be seen in the next section, this peak is of a crucial importance for our present study. The differences between the various datasets, especially for strong narrow peaks of IS0 strength, can most likely be ascribed to differences in the experimental energy resolution and a subtle interplay between binning effects and differences in the calibration of the excitation energy.

As for ^{28}Si (Fig. 6), the iThemba LABS results are mainly consistent with the previous findings by the TAMU group, except for a slightly lower value of the IS0 strength at the peak of the distribution. The results from RCNP, on the other hand, exhibit almost a factor of two larger IS0 strength above 19 MeV than both the iThemba LABS and the TAMU results. One should also

note that some of the IS0 strength at lower excitation energy might not belong to the ISGMR. It was suggested that, in ^{28}Si , the 0^+ states at 9.71 MeV, 10.81 MeV, 11.14 MeV, and 12.99 MeV, i.e. most of the IS0 strength below 15 MeV, can be considered as potential band heads for superdeformed bands [22].

With the good energy resolution of the present experiment, $J^\pi = 0^+$ states could be resolved up to 16 MeV in ^{24}Mg and 15 MeV in ^{28}Si . The corresponding strengths $S(\text{IS0})$ and % EWSR exhausted by the strongest discrete states evident in Fig. 4 are summarised in Tables III and IV, respectively. The values obtained in this study are in good agreement with results from Ref. [21] which analysed angular distributions of individual states, employing a different DWBA code as well as OMPs.

IV. QRPA CALCULATIONS AND COMPARISON WITH EXPERIMENT

A. Details of the calculations

The calculations were performed within the QRPA model [39–42] based on the Skyrme functional [43, 44]. The model is fully self-consistent. Both the mean field and the residual interaction are derived from the initial Skyrme functional. The residual interaction takes into account all the terms following from the Skyrme functional and Coulomb (direct and exchange) parts. Both particle-hole and particle-particle channels are included [40]. Pairing is treated at the BCS level [40]. Spurious admixtures caused by pairing-induced violation of the particle number are removed using the method from Ref. [42].

A representative set of Skyrme forces is used, see Table V. For our aims, the most important characteristics of the forces are the nuclear incompressibility K_∞ and the isoscalar effective mass m_0^*/m affecting ISGMR and ISGQR energies, respectively. The corresponding values are listed in Table V. We employ the standard force SkM* [45] and the most recent force SV-bas [46]. Both forces were previously used in the analysis presented in [12–14, 16]. Further, we use the earlier force SkT6 [47] and more recent force SV-mas10 [46] which both have a large effective mass, $m_0^*/m = 1$, and so are favourable for the description of the ISGQR [10, 48, 49]. Finally, we exploit the force SkP $^\delta$ [50] which has a very low incompressibility $K_\infty = 202$ MeV. In a recent study of the ISGMR in Mo isotopes, this force gave the best results [10].

The nuclear mean field and pairing are computed by the code SKYAX [51] using a two-dimensional grid in cylindrical coordinates. The calculation box extends up to three nuclear radii and the grid step size is 0.4 fm. The axial quadrupole equilibrium deformation is obtained by minimisation of the energy of the system. As shown in Fig. 7, both ^{24}Mg and ^{28}Si have oblate and prolate minima. However, in the ground state, ^{24}Mg is prolate and

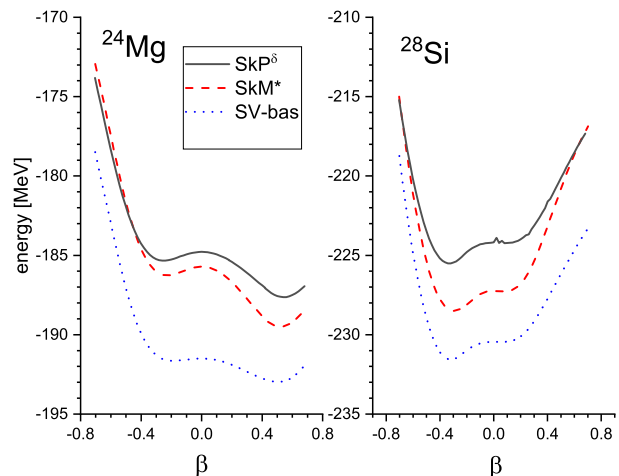


FIG. 7: Total energy of ^{24}Mg (left) and ^{28}Si (right), calculated in the framework of QRPA with the forces SkP $^\delta$, SkM* and SVbas as a function of the deformation parameter β .

^{28}Si is oblate. As shown in Table VI, the calculated deformation parameters β somewhat underestimate the experimental values [38]. This is typical for light deformed nuclei, see e.g. Ref. [52]. For all the applied Skyrme forces, the pairing in ^{24}Mg and ^{28}Si was found to be very weak. This is explained by the sparse single-particle spectrum in light nuclei.

The calculations use a large configuration space. The single-particle spectrum extends from the bottom of the potential well up to 30 MeV. For example, SkP $^\delta$ calculations use 404 proton and 404 neutron single-particle levels for ^{24}Mg and 422 proton and 422 neutron single-particle levels for ^{28}Si . The two-quasiparticle (2qp) basis in QRPA calculations with SkP $^\delta$ extends up to 70 MeV. It includes 1056 proton and 956 neutron $K^\pi = 0^+$ states in ^{24}Mg and 1142 proton and 1002 neutron states in ^{28}Si . The isoscalar monopole energy-weighted sum rule $\text{EWSR}(\text{IS0}) = 2\hbar^2/m \cdot A\langle r^2 \rangle_0$ is exhausted by 97 – 99%.

QRPA strength functions for isoscalar monopole ($L = 0$) and quadrupole ($L = 2$) transitions have the form

$$S_L(E) = \sum_{K=0}^L (2 - \delta_{K,0}) \sum_{\nu \in K} |\langle \nu | \hat{O}_{LK} | 0 \rangle|^2 \xi_\Delta(E - E_\nu), \quad (5)$$

where ν labels QRPA eigenvalues $|\nu\rangle$ with energies E_ν , and $|0\rangle$ is the QRPA ground state. The monopole and quadrupole isoscalar transition operators are $\hat{O}_{00} = \sum_i^A r_i^2$ and $\hat{O}_{20} = \sum_i^A r_i^2 Y_{20}(\hat{r}_i)$, respectively. For convenient comparison with the experimental data, the strength is smoothed by a Lorentz function $\xi_\Delta(E - E_\nu) = \Delta / (2\pi[(E - E_\nu)^2 - \Delta^2/4])$ with an averaging parameter $\Delta = 1$ MeV. The dimension of the strength functions is fm^4/MeV . We also present 2qp strength functions calculated without the residual interaction. In this case, the number ν in Eq. (5) labels 2qp states.

TABLE III: Excitation of prominent $J^\pi = 0^+$ states in ^{24}Mg . $S(\text{IS0})$ is the experimental IS0 strength exhausted by the state.

E_x (MeV) ^a	E_x (MeV) ^b	E_x (MeV) ^c	% EWSR ^a	% EWSR ^c	$S(\text{IS0})$ (fm ⁴) ^a
9.31(1)	9.30539(24)		1.0(1)	1.4(3)	19.9(20)
10.68(1)	10.6797(4)		0.31(5)	0.29(6)	5.32(61)
11.73(1)	11.7281(10)		0.77(11)	1.0(2)	12.1(16)
13.36(2)		13.37(1)	0.40(5)	0.5(1)	4.32(71)
		13.79(1)		1.7(3)	
13.87(2) ^d	13.884(1)	13.89(1)	2.8(3) ^d	2.6(5)	37.7(38) ^d
15.32(2)		15.33(3)	1.7(2)	1.9(4)	20.7(25)
15.78(2)		15.79(3)	0.40(5)	1.1(2)	4.6(10)

^aPresent experiment.^bFrom Ref. [38].^cFrom Ref. [21].^dThe integration region for the 13.87(2) state from the present experiment includes both the 13.79 MeV and 13.89 MeV states from Ref. [21].TABLE IV: Same as in Table III but for excitation of $J^\pi = 0^+$ states in ^{28}Si .

E_x (MeV) ^a	E_x (MeV) ^b	% EWSR ^a	% EWSR ^b	$S(\text{IS0})$ (fm ⁴) ^a
9.70(2)	9.71(2)	0.22(4)	0.38(8)	5.2(6)
10.81(2)	10.81(3)	0.27(4)	0.35(7)	5.7(6)
11.14(2)	11.142(1)	0.8(1)	0.9(2)	15.3(17)
13.00(2)	12.99(2)	0.95(12)	0.8(2)	16.9(18)
15.03(3)	15.02(3)	0.40(9)	0.8(2)	6.0(15)
15.77(3)		0.7(1)		9.7(16)

^aPresent experiment.^bFrom Ref. [22].

B. Strength distribution and IS0/IS2 coupling

The QRPA IS0 strength functions from Eq. (5) are compared with the experimental data in Figs. 8 - 11. The

TABLE V: Incompressibility K_∞ and isoscalar effective mass m_0^*/m for the Skyrme forces SV-bas, SkM*, SkP ^{δ} , SkT6 and SV-mas10 used in the present analysis.

	SV-bas	SkM*	SkP ^{δ}	SkT6	SV-mas10
K_∞ (MeV)	234	217	202	236	234
m_0^*/m	0.9	0.79	1	1	1

TABLE VI: Experimental and calculated deformation parameters β in ^{24}Mg and ^{28}Si .

	Exp. ^a	SV-bas	SkM*	SkP ^{δ}	SkT6	SV-mas10
^{24}Mg	0.613	0.527	0.522	0.545	0.506	0.518
^{28}Si	-0.412	-0.308	-0.291	-0.322	-0.311	-0.295

^aFrom Ref. [38].

iThemba LABS experimental data are shown by black filled circles where each data point accumulates the IS0 strength in an energy interval of 0.5 MeV.

In Fig. 8, the strength functions calculated with the force SV-bas are shown. In our set of Skyrme forces, SV-bas has a large (though rather typical for Skyrme forces) incompressibility $K_\infty = 234$ MeV. The calculated QRPA IS0 strengths (blue solid line) in ^{24}Mg and ^{28}Si are separated into a narrow structure at ~ 14 MeV in ^{24}Mg and ~ 18 MeV in ^{28}Si and a broad structure at

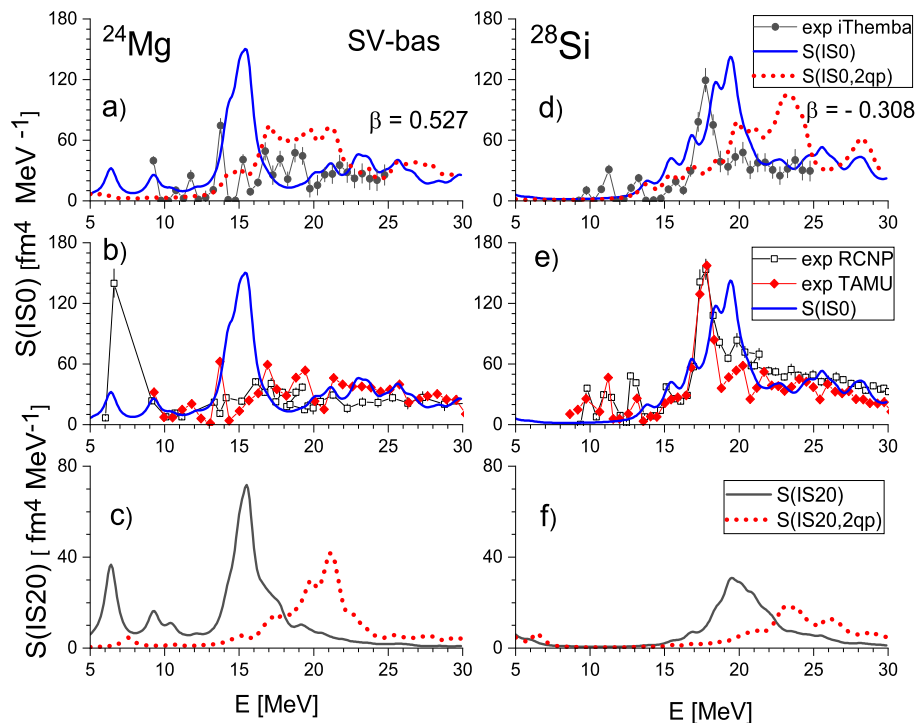


FIG. 8: Upper panels: QRPA (solid black line) and 2qp (short-dash red line) IS0 strength functions calculated with the force SVbas ($K_\infty = 234$ MeV) in ^{24}Mg (left) and ^{28}Si (right) and comparison with the present iThemba LABS experimental data shown as black filled circles. Middle panels: comparison with RCNP [14, 16] (black empty squares) and TAMU [18, 19] (red filled diamonds) experimental data. Bottom panels: QRPA (solid black line) and 2qp (short-dash red line) IS20 strengths.

higher energy, which is a typical picture for deformed nuclei [9]. It is instructive to compare QRPA IS0 strength with the 2qp IS0 one (red dashed line) obtained without the residual interaction. We see a strong collective effect: the residual interaction essentially shifts down the IS0 strength and creates collective peaks at ~ 14 MeV in ^{24}Mg and ~ 18 MeV in ^{28}Si .

The bottom panels of Fig. 8 show the $LK = 20$ branches of the ISGQR (see Appendix A for discussion of the deformation splitting of the ISGQR in prolate and oblate nuclei) in the QRPA and 2qp cases. Here, we also observe a strong collective effect. Additionally, one observes that the main IS20 QRPA peak lies at the same energy as the narrow IS0 QRPA peak. Thus, both peaks are related, i.e., we observe a clear deformation-induced coupling of the IS0 and IS20 modes. The larger the nuclear deformation, the more strength is concentrated in the narrow IS0 peak [9]. Altogether, we see that the narrow IS0 peaks in ^{24}Mg and ^{28}Si have a dual (collective effect + deformation-induced IS0/IS20 coupling) origin.

Now the question arises which structures in the experimental data should be associated with the calculated IS0 narrow peak. To inspect this point, let us consider in Fig. 8 the experimental data from iThemba LABS (upper panel), RCNP [14, 16] and TAMU [18, 19] (middle panel). In ^{28}Si , all the data give a distinctive strong narrow peak at 17–19 MeV. In ^{24}Mg , the issue is more complicated. Here, the iThemba LABS and TAMU data give

a distinctive narrow peak at 13–14 MeV but the RCNP data [14] do not. At the same time, a hump at 13–14 MeV also appears in the (^6Li , $^6\text{Li}'$) data [17]. Moreover, it is clearly observed at 13.8 MeV in the RCNP (α , α') data of Ref. [15], which have an energy resolution comparable to the present experiment. Finally, the narrow peak at 13–14 MeV was observed in early (α , α') [36] and (^6Li , $^6\text{Li}'$) [37] experiments. So, in ^{24}Mg , the peak at 13–14 MeV is a good candidate for the comparison with the narrow IS0 peak in our QRPA calculations and the analysis of IS0/IS2 coupling.

Note that the proper choice of the experimental IS0 peak for the comparison with theory is of crucial importance in the present study. As argued above, this peak arises due to IS0/IS2 coupling in deformed nuclei and its energy location can be used to find the optimal Skyrme force and thereby determine the relevant incompressibility K_∞ and isoscalar effective mass m_0^*/m . In Ref. [14], the local maximum at 16–17 MeV was assumed to be the narrow peak, which resulted in the preference of the force SkM* ($K_\infty = 217$ MeV, $m_0^*/m = 0.79$). Below we will show that in ^{24}Mg , the experimental peak at 13–14 MeV in the iThemba LABS and TAMU data is a better suited candidate. This will change the predicted values of K_∞ and m_0^*/m .

To justify the latter, let us compare the calculated and experimental IS0 strengths in Fig. 8. It is seen that the calculated narrow IS0 peaks lie higher by 1.5–2 MeV

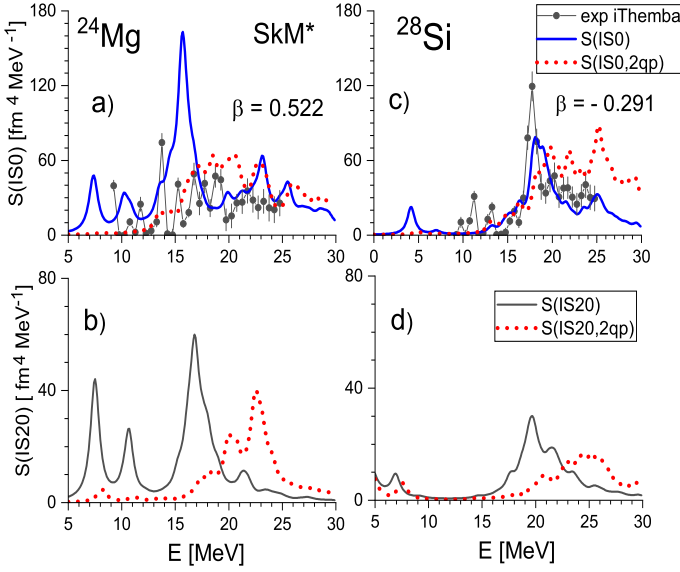


FIG. 9: Same as upper and lower panels of Fig. 8 but for the force SkM* with $K_\infty = 217$ MeV.

than the experimental peaks at 13.8 MeV (^{24}Mg) and about 18 MeV (^{28}Si). If we additionally upshift the calculated IS0 strength in both nuclei, we could match the RCNP structure at 16 – 17 MeV in ^{24}Mg but, simultaneously, would essentially worsen the description of the strength in ^{28}Si . Instead, if we assume the 13.8 MeV peak as the relevant narrow structure in ^{24}Mg , then it remains possible to describe IS0 results in ^{24}Mg and ^{28}Si consistently by an equal downshift of the QRPA narrow peaks.

Figure 8 shows that SV-bas generally well describes the main ISGMR located at 16 – 25 MeV in ^{24}Mg and 20 – 25 MeV in ^{28}Si . The only noticeable discrepancy is that the theory noticeably underestimates IS0 strength at 16 – 20 MeV in ^{24}Mg where the experiment shows a sequence of prominent peaks. This discrepancy can be caused by the disregard in our calculations of the Coupling with Complex Configurations (CCC). The CCC could redistribute the strength, reducing the height of the narrow IS0 peak and shifting a part of its strength to the range 16 – 20 MeV.

Previous work has shown that the lower K_∞ , the smaller the ISGMR centroid energy [3, 9]. In Fig. 8, SV-bas gives IS0 narrow peaks at too high excitation energy. So it is worth to try a force with a smaller K_∞ . In Fig. 9, results for the SkM* force with $K_\infty = 217$ MeV are shown. As in Fig. 8, we see a strong collective effect. The energy of the narrow IS0 peak again coincides with the energy of the quadrupole $LK = 20$ branch, which means that this peak is produced by the IS0/IS2 coupling. However, SkM* does not improve the results: the energy of the IS0 narrow peak is still noticeably overestimated. The downshift of the IS0 strength due to the smaller $K_\infty = 217$ MeV is countered by an upshift due to the smaller value of the effective mass $m_0^*/m = 0.79$

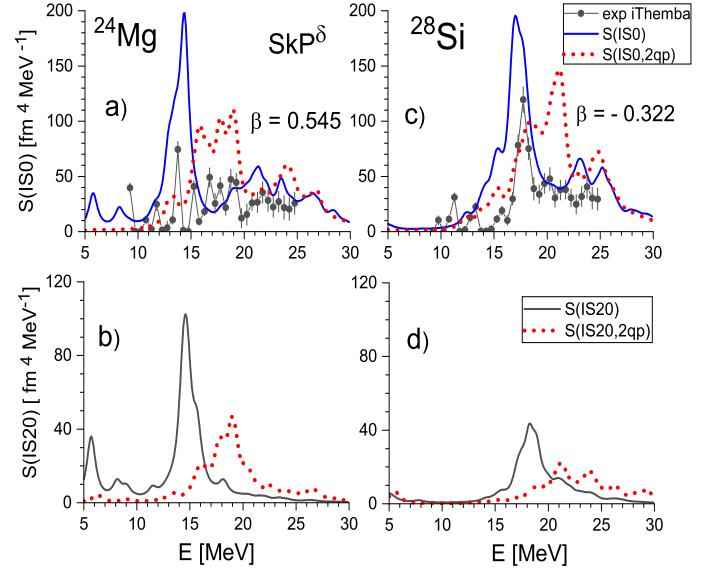


FIG. 10: Same as in Fig. 9 but for the force SkP $^\delta$ with $K_\infty = 202$ MeV.

(see the discussion of the impact of the effective mass, in connection with Fig. 12).

Next, in Fig. 10, we present results for the force SkP $^\delta$ with a low incompressibility $K_\infty = 202$ MeV and high effective mass $m_0^*/m = 1$. Now both factors downshift the IS0 strength as compared with the SV-bas case. An improved agreement with the experimental IS0 strength distributions is observed: both in ^{24}Mg and ^{28}Si the calculated IS0 narrow peaks now match the experimental structures. Note that SkP $^\delta$ also provides the best description of the ISGMR in deformed Mo isotopes [10]. In Fig. 10, the narrow peaks are again produced by IS0/IS2 coupling and a strong collective effect takes place.

In Figs. 8 - 10, the quadrupole IS20 peak in ^{24}Mg is stronger and has a lower energy than in ^{28}Si . As a result, the narrow IS0 peak in ^{24}Mg is more separated from the main ISGMR than in ^{28}Si . This is explained by the larger absolute quadrupole deformation of ^{24}Mg as compared with ^{28}Si , which results in a stronger downshift of the IS20 peak in ^{24}Mg . Besides, Figs. 8 - 10 show that IS0/IS2 coupling is relevant also for lower-energy states.

Due to the IS0/IS2 coupling, the energy of the narrow peak is sensitive to the isoscalar effective mass m_0^*/m which affects the ISGQR energy [10, 48]. In general, the larger m_0^*/m , the smaller the ISGQR centroid energy [48]. So, in principle, one can try to downshift the energy of the narrow IS0 peak solely using a large value of m_0^*/m . In Fig. 11, the forces SkT6 ($K_\infty = 236$ MeV) and SV-mas10 ($K_\infty = 234$ MeV), which both have an effective mass $m_0^*/m = 1$, are applied for the calculation of the IS0 strength. It is seen that these two forces still overestimate the energies of the narrow IS0 peaks like in the cases of SV-bas and SkM*. Thus, the optimum Skyrme force also needs a lower value of K_∞ .

We note that a QRPA calculation of the ISGMR

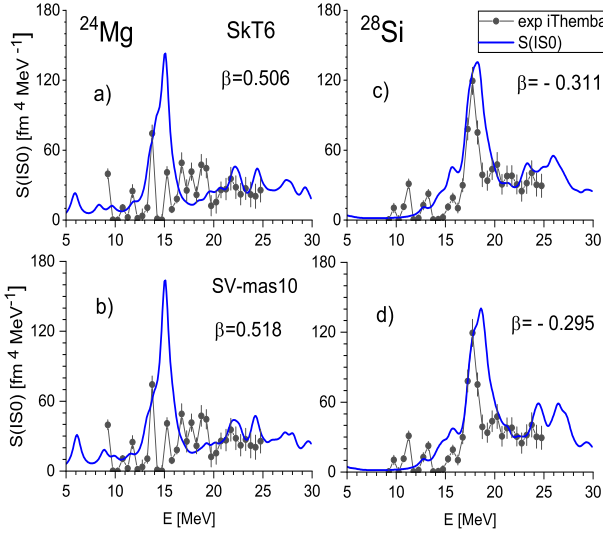


FIG. 11: QRPA IS0 strength functions (solid lines) calculated with the Skyrme forces SkT6 (upper panels) and SV-mas10 (bottom panels).

strength in ^{24}Mg with a Gogny force is discussed in Ref. [17]. There, a reasonable agreement with the data could only be achieved after an ad-hoc upshift of the IS0 strength distribution by 2 MeV.

C. IS2 strength

Since the energy of the narrow monopole peak is determined by the $K = 0$ branch of the ISGQR, it is important to consider the ISGMR and ISGQR simultaneously. In particular, we should see how well we can describe the ISGQR and its deformation splitting in ^{24}Mg and ^{28}Si . This is investigated in Appendix A for various values of the deformation parameter β . For ^{24}Mg , only prolate deformations are inspected. For ^{28}Si , where oblate and prolate deformations for excited states were predicted [22, 53–55], both types of deformations are considered. In ^{24}Mg , the calculations show the behaviour expected for prolate deformation splitting where the energies of the branches $LK = 20, 21$, and 22 follow the relation $E_{20} < E_{21} < E_{22}$. The branch $LK = 20$ is strong. It is downshifted by 4–5 MeV when increasing the deformation from $\beta = 0.1$ to 0.522. The same splitting features are seen in prolate ^{28}Si . However, in oblate ^{28}Si , the deformation splitting of ISGQR looks surprising. The branch $LK = 20$ is not upshifted, as would be expected, but downshifted (by 3–4 MeV from $\beta = -0.1$ to -0.412) and becomes rather weak.

These features of the deformation splitting are illustrated in Fig. 12, where SkM*, SV-bas and SkP $^\delta$ QRPA results are compared with ISGQR data obtained in the reactions ($^6\text{Li}, ^6\text{Li}'$) for ^{24}Mg [17] and (α, α') for ^{28}Si [19]. For better visibility, the experimental values for ^{28}Si are multiplied by a factor of 10. All three forces reasonably

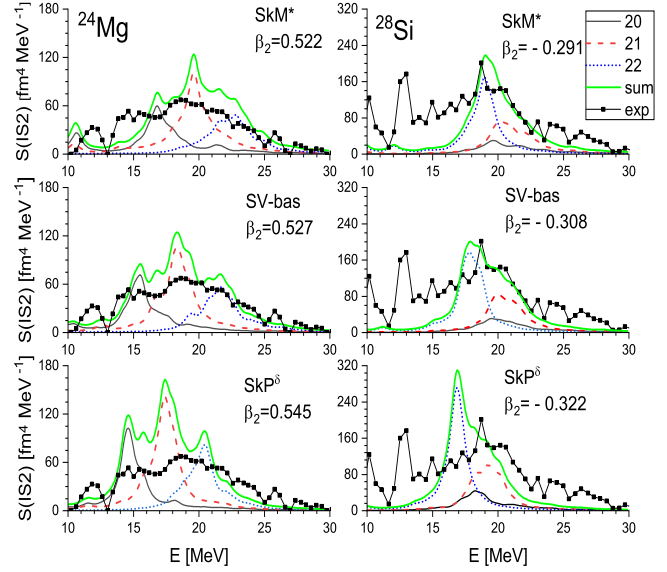


FIG. 12: ISGQR in ^{24}Mg (left) and ^{28}Si (right), calculated with the forces SkM* (upper panels), SV-bas (middle panels) and SkP $^\delta$ (bottom panels). Energy-weighted strength functions $S(\text{IS}2)$ for the branches $LK = 20$ (thin solid black line), 21 (dashed red line) and 22 (dotted blue line) as well as for the summed 20+21+22 strength (bold green line) are shown. The experimental data are taken from Ref. [17] for ^{24}Mg and Ref. [19] for ^{28}Si . For better visibility, the latter are multiplied by a factor of 10.

reproduce the IS2 experimental data. In ^{24}Mg , the best description is obtained with SV-bas. In ^{28}Si , SkM* and SV-bas give reasonable results. It is seen that the humps of the experimental strength at 14 and 19 MeV in ^{24}Mg are produced by the $LK = 20$ and 21 branches, respectively. In ^{28}Si , the main peak at 19 MeV is produced by the $LK = 22$ branch. Figure 12 demonstrates a regular dependence of the ISGQR features on increasing the isoscalar effective mass m_0^*/m from 0.79 (SkM*) to 0.9 (SV-bas) to 1.0 (SkP $^\delta$). The larger the value of m_0^*/m , the stronger the deformation (and the deformation splitting) and the larger the energy downshift of the ISGQR. The force SkP $^\delta$, being best in description of the ISGMR, turns out to be not very good for the ISGQR. A consistent description of the ISGMR and ISGQR would need a Skyrme force with $m_0^*/m \approx 0.9$ and $K_\infty < 217$ MeV (the same conclusion was drawn earlier in the study of ISGMR/ISGQR in Mo isotopes [10]). The forces used above do not fulfil these requirements.

Note that our QRPA IS2 strength functions are computed for band heads $I^\pi K = 0^+0, 1^+1, 2^+2$ while IS2 experimental data are obtained for the states $I^\pi K = 2^+0, 2^+1, 2^+2$, i.e. for rotational states in $K = 0$ and 1 cases. So, for a more accurate comparison with the experiment, the calculated IS2 ($K = 0, 1$) strengths should be shifted to a higher energy by the rotational correction. It can be estimated roughly from the energy of the 2^+0 state in the ground-state rotational band, which is 1.368

MeV for ^{24}Mg and 1.779 MeV for ^{28}Si [38]. Though the corrections are significant, they do not affect the conclusions drawn from Fig. 12.

D. Integral IS0 strength

For further comparison, it is worth considering the integrated IS0 strengths $\sum_{\nu} B_{\nu}(\text{IS0})$ in the energy range 9 – 25 MeV covered by the present experiment. Here, $B_{\nu}(\text{IS0}) = |\langle \nu | \hat{O}_{2K} | 0 \rangle|^2$ is the reduced probability of the IS0 transition from the ground to ν -th QRPA state. The results for the main three forces used in the present study (SkP $^{\delta}$, SkM* and SV-bas) are shown in Table VII. One observes an anticorrelation between K_{∞} and $\sum_{\nu} B_{\nu}(\text{IS0})$: the calculated $\sum_{\nu} B_{\nu}(\text{IS0})$ steadily decreases from SkP $^{\delta}$ to SV-bas, i.e. with increasing K_{∞} from 202 MeV to 234 MeV. As demonstrated for the strength distributions in Figs. 8 - 11, the best agreement with experiment is obtained for the force SkP $^{\delta}$. Indeed, this force gives a reasonable reproduction of the summed strength in ^{24}Mg (together with the force SkM*) and the best reproduction of the summed strength in ^{28}Si . Besides, SkP $^{\delta}$ describes well the peak energy E_p of the narrow IS0 resonance in ^{24}Mg and reasonably in ^{28}Si . So, with this force, we simultaneously describe the energy of the narrow IS0 peak and integral strength $\sum_{\nu} B_{\nu}(\text{IS0})$. To the best of our knowledge, this is achieved for the first time.

It is also interesting to inspect contributions of IS0 strength from different energy intervals to the energy-weighted sum rule $\text{EWSR} = 2\hbar^2/m \cdot A \langle r^2 \rangle_0$ summarised in Table VIII. It is seen that the experimental strengths exhaust about 70% of the EWSR in ^{24}Mg and 77% in ^{28}Si . The forces SkP $^{\delta}$, SkM* and SV-bas give rather similar results. All calculations exhaust close to 100% EWSR in the model space 0 – 70 MeV. In ^{24}Mg , the calculations

TABLE VII: Peak energy E_p of the narrow IS0 resonance and summed strength $\sum_{\nu} B_{\nu}(\text{IS0})$ in the energy interval 9 – 25 MeV from various Skyrme forces compared with the present experimental data.

	^{24}Mg			^{28}Si	
	K_{∞}	E_p	$\sum B(\text{IS0})$	E_p	$\sum B(\text{IS0})$
	(MeV)	(MeV)	(fm 4)	(MeV)	(fm 4)
Exp.		13.75(2)	728(41)	17.75(3)	895(40)
SkP $^{\delta}$	202	14.3	796	17.0	908
SkM*	217	15.6	706	18.0	780
SVbas	234	15.4	634	19.4	685

overestimate the experimental strength at 0 – 16 MeV (low-energy IS0 strength and the narrow peak) and underestimate it at 16 – 25 MeV (main part of ISGMR). It seems that the Skyrme forces redistribute too much strength from the main ISGMR to the narrow IS0 peak. A large part of the strength, 25 – 37%, is located above 25 MeV, i.e. beyond the scope of the iThemba LABS experiment. For ^{28}Si , the agreement of the experiment and theory is much better. The calculations reproduce rather well a small strength at 0 – 25 MeV and its major part at 16 – 25 MeV.

E. Features of individual IS0 transitions

The energy range 9 – 25 MeV embraces many QRPA 0^+ states. For example, in the SkP $^{\delta}$ case, we have 631 states in ^{24}Mg and 537 states in ^{28}Si . It is instructive to consider in more detail QRPA states which form the narrow IS0 peak and strong IS0 excitations at a lower energy. In Table IX, the characteristics of IS0 states in the energy range 5 – 18 MeV with a strength $B(\text{IS0}) > 40 \text{ fm}^4$ are presented. In ^{24}Mg , there are two transitions with a large monopole strength below 13 MeV. The three transitions at energies between 13.5 MeV and 14.5 MeV form the strong narrow IS0 peak shown in Fig. 10. Following our calculations, two of these states, at 14.3 and 14.5 MeV, are very collective (composed by many 2qp components with the largest 2qp contributions to the state norm as 40% and 48%, respectively), which justifies the collective effect mentioned above. Most probably just these two states with close energies correspond to the 13.87 MeV level from the iThemba LABS data (see Table III). It is difficult to establish one-to-one correspondence between the measured transitions in Table III and calculated transitions in Table IX since our Skyrme QRPA calculations neglect some important effects (coupling with complex configurations and shape coexistence) and thus have not enough accuracy for such a detailed comparison. For ^{24}Mg and ^{28}Si , there are attempts of one-to-one comparison of the experimentally observed discrete 0^+ -levels using Gogny QRPA [17] and Antisymmetrised Molecular Dynamics (AMD) [56] calculations. However, these calculations achieve a reasonable agreement with the data using only an ad-hoc upshift of the IS0 strength distribution by 2 MeV.

All the states in Table IX have large values for $0_{\text{gs}}^+ \rightarrow 2^+_{0\nu}$ isoscalar quadrupole transitions with $\Delta K = 0$. This once more confirms the strong IS0/IS2 coupling in strongly prolate ^{24}Mg . The main IS0 resonance at 18 – 25 MeV (not considered in Table IX) is formed by a large number of mildly collective states with $B(\text{IS0}) < 1 \text{ fm}^4$. The results for strongly oblate ^{28}Si generally agree with those for ^{24}Mg . However, as seen from Table IX, in ^{28}Si our calculations do not predict monopole states with a high $B(\text{IS0})$ and $B(\text{IS2}, K = 0)$ below 15 MeV.

TABLE VIII: Energy-weighted strengths $\sum_{\nu} E_{\nu} B_{\nu}(\text{IS0})$ for ^{24}Mg and ^{28}Si , summed in the energy intervals 0 – 16 MeV, 16 – 25 MeV, 25 – 70 MeV, and 0 – 70 MeV. The strengths are given in % of the monopole EWSR (see text for more detail). In the interval 0 – 16 MeV, the experimental strength is measured only in the interval 9 – 16 MeV.

	^{24}Mg				^{28}Si			
	0 – 16	16 – 25	25 – 70	0 – 70	0 – 16	16 – 25	25 – 70	0 – 70
Exp.	15(1)	55(4)	0	70(4)	7(1)	68(4)	0	75(4)
SkP $^{\delta}$	38	35	25	98	11	63	25	97
SkM*	31	37	29	97	5	64	29	98
SV-bas	35	25	37	97	6	55	38	99

TABLE IX: Characteristics of low-energy $K^{\pi} = 0^{+}$ states with excitation energy $E_{\nu} > 5$ MeV and reduced transition probability $B(\text{IS0}) > 40 \text{ fm}^4$ in ^{24}Mg and ^{28}Si , calculated within QRPA with the force SkP $^{\delta}$. For each state, we show the excitation energy, the reduced transition probabilities $B(\text{IS0})$ and $B(\text{IS20})$, and the main 2qp components (contribution to the state norm in %, and structure in terms of Nilsson asymptotic quantum numbers).

Nucleus	E_{ν} (MeV)	$B(\text{IS0})$ (fm^4)	$B(\text{IS20})$ (fm^4)	main 2qp components %	main 2qp components [N, n_z, Λ]
^{24}Mg	5.8	51	56.5	49	pp [220 \uparrow -211 \downarrow]
	12.9	75	11.7	96	pp [211 \uparrow -431 \uparrow]
	13.5	77	26.5	92	pp [220 \uparrow -440 \uparrow]
	14.3	166	77.1	40	pp [211 \uparrow -411 \uparrow]
	14.5	81	40.0	48	pp [211 \uparrow -411 \uparrow]
^{28}Si	15.3	42	3.0	91	pp [200 \uparrow -431 \downarrow]
	16.6	59	7.1	90	pp [202 \uparrow -413 \downarrow]
	16.9	91	10.5	68	nn [200 \uparrow -411 \downarrow]
	17.3	47	4.3	39	nn [200 \uparrow -420 \uparrow]
	17.6	62	6.0	75	pp [202 \downarrow -431 \uparrow]
	17.8	82	18.8	22	pp [200 \uparrow -600 \uparrow]

F. Cluster features of the narrow IS0 peak in ^{24}Mg

The strong narrow peak at 13.87 MeV in ^{24}Mg lies close to the thresholds of cluster configurations $^{12}\text{C}+^{12}\text{C}$ and $^{16}\text{O} + 2\alpha$ and, following the coincidence experiment [15], should exhibit cluster features. To check this point, we calculated the density distribution of the QRPA 14.3 MeV 0^{+} state (assuming correspondence to the observed 13.87 MeV excitation) and compared it with the density of the ground state. In Fig. 13, both densities are exhibited in the $x - z$ plane where z is the symmetry axis. Another relevant collective 0^{+} state at 14.5 MeV has a similar density contribution and so is not considered here.

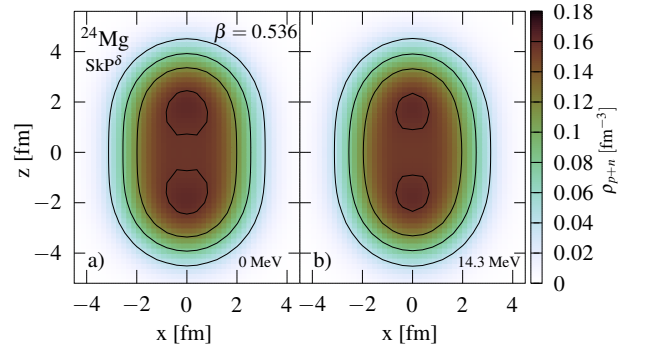


FIG. 13: Density profiles in $x - z$ plane, calculated with the force SkP $^{\delta}$ in ^{24}Mg for the ground state (left) and excited QRPA $K^{\pi} = 0^{+}$ state at 14.3 MeV (right).

In the ground state, prolate ^{24}Mg has two spots of the enhanced density in the pole regions. These spots persist, though being somewhat shrunk, in the 14.3 MeV 0^{+} state. The density spots can be considered as precursors of clustering. They can be treated as predecessors of two ^{12}C clusters or, to a lesser extent, of two α -particles with ^{16}O . Note that the plot for 14.3 MeV state agrees well with the $^{12}\text{C}+^{12}\text{C}$ density plots in Ref. [56] where the cluster features of ^{24}Mg are analysed within the AMD method. The similarity of the density plots for the ground and excited states can be explained by a dual nature (mean field + clustering) of the ground state of light nuclei, see the discussion and further citation in Ref. [56]. Altogether we see that the strong narrow IS0 peak in ^{24}Mg might combine both mean-field (IS0/IS2 coupling) and cluster features. The nucleus ^{28}Si also demonstrates cluster properties (see e.g. discussions in Refs. [21, 53]). However analysis of these properties is complicated by the shape coexistence in this nucleus and so is skipped here.

V. CONCLUSIONS

The isoscalar monopole strength in the energy interval $9 \leq E_x \leq 25$ MeV in ^{24}Mg and ^{28}Si has been investigated using α -particle inelastic scattering with a 196 MeV beam at scattering angles $\theta_{\text{Lab}} = 0^\circ$ and 4° . The K600 magnetic spectrometer and the Separated Sector Cyclotron (SSC) at iThemba LABS were used.

The DoS technique was applied in order to extract the IS0 strength distributions. The difference spectrum obtained for each nucleus was converted to the fraction of the IS0 EWSR per bin and compared with MDA analysis results obtained by the TAMU [18, 19] and RCNP [12, 14–17] groups. Overall, the strength distributions obtained in this study show a reasonable agreement with results from both groups, with exception of the RCNP data [12, 14] for IS0 structures in the energy range 13–18 MeV in ^{24}Mg . At the same time, we find good agreement for this energy range with another (α, α') experiment performed at RCNP [15].

The extracted IS0 strength distributions were compared to calculations performed in the framework of QRPA. A representative set of Skyrme forces (SkM*, SV-bas, SkP $^\delta$, SkT6 and SV-mas10) with different incompressibility K_∞ values and isoscalar effective masses m_0^*/m was used. Similar to a recent study for Mo isotopes [10], the present iThemba LABS experimental data for the ISGMR in ^{24}Mg and ^{28}Si are best described by the force SkP $^\delta$ with a low incompressibility $K_\infty = 202$ MeV. This force allows the reproduction of both i) the energy of the narrow IS0 peaks at 13.8 MeV in ^{24}Mg and 18 MeV in ^{28}Si and ii) the integral IS0 strengths $\sum B(\text{IS0})$.

In the theoretical analysis, the main attention was paid to the narrow IS0 peak constituting a convenient and sensitive test case to determine the nuclear incompressibility in deformed nuclei. The comparison of IS0 and IS2 strength distributions justifies that the narrow IS0 peak appears due to the deformation-induced coupling between the ISGMR and the $K = 0$ branch of the ISGQR. The important role of a large collective downshift of the IS0 strength (due to the isoscalar residual interaction) in the production of the narrow IS0 peak is demonstrated. In ^{24}Mg , the narrow IS0 peak lies close to the $^{12}\text{C}+^{12}\text{C}$ threshold [15] and so, in accordance with our analysis and observations [15], can demonstrate cluster features.

In connection with the strong IS0/IS2 coupling effect, we also performed a detailed analysis of the ISGQR in ^{24}Mg and ^{28}Si . An unusual deformation splitting in oblate ^{28}Si was found. The calculations show that the quadrupole $K = 0$ branch is strongly downshifted in prolate ^{24}Mg and slightly downshifted in oblate ^{28}Si . This explains why the narrow IS0 peak is well separated from the main ISGMR in ^{24}Mg but superimposed on the broad structure of the main ISGMR in ^{28}Si .

Our analysis demonstrates that the ISGMR in deformed nuclei must be described simultaneously with the ISGQR. Only then can such a description be consid-

ered as relevant and consistent. In our calculations, the Skyrme force SkP $^\delta$ gives the best results for a simultaneous reproduction of ISGMR and ISGQR. However, even this force has shortcomings for the description of the ISGQR. There is a need for new Skyrme parameterisations with $K_\infty < 217$ MeV and $m_0^*/m \approx 0.9$.

ACKNOWLEDGEMENTS

The authors thank the Accelerator Group at iThemba LABS for the high-quality dispersion-matched beam provided for this experiment. A.B. acknowledges financial support through iThemba LABS, NRF South Africa. R.N. acknowledges support from the NRF through Grant No. 85509. The authors thank Prof P.-G. Reinhard for the code SKYAX. This work was supported by the Deutsche Forschungsgemeinschaft under contract SFB 1245 (Project ID No. 79384907) and NRF-JINR grant JINR200401510986. V.O.N. and J.K. acknowledge the Votruba - Blokhintsev (Czech Republic - BLTP JINR) grant. J.K. appreciates the support by a grant of the Czech Science Agency, Project No. 19-14048S. V.O.N. and P.v.N.-C. appreciate the support by a Heisenberg-Landau grant (Germany - BLTP JINR). A.R. acknowledges support by the Slovak Research and Development Agency under Contract No. APVV-20-0532 and by the Slovak grant agency VEGA (Contract No. 2/0067/21). P. A. acknowledges support from the Claude Leon Foundation in the form of a postdoctoral fellowship.

Appendix A: ISGQR in ^{24}Mg and ^{28}Si

As shown in the main text, the $K = 0$ branch of the ISGQR determines the energy of the narrow IS0 peak. The energy of this branch is governed by the deformation splitting of the ISGQR into $K = 0, 1$ and 2 components. So, it is worthwhile to investigate the deformation splitting of the ISGQR in ^{24}Mg and ^{28}Si in more detail. Figure 14 shows the strength distributions of the branches for different axial quadrupole deformations. The calculations are performed for the parametrisation SkM* as an example but other forces lead to the same qualitative conclusions.

In the plots a)-d), the ISGQR strength distribution in prolate ^{24}Mg is exhibited at $\beta = 0.1, 0.3, 0.522$ (calculated equilibrium value) and 0.613 (experimental value). We see a splitting picture typical for prolate nuclei: the $K = 0$ branch is downshifted from 21 MeV ($\beta = 0.1$) to 16 MeV ($\beta = 0.613$), the $K = 1$ branch shows less downshift from 21 to 19 MeV, and the $K = 2$ branch is upshifted from 22 to 23 MeV. The energy of the $K = 0$ branch is most sensitive to the deformation. However, even at $\beta = 0.613$, this branch does not approach an excitation energy 13 – 14 MeV where experiment gives the narrow monopole peak. So, to describe the experimental data we need a force like SkP $^\delta$ with a smaller

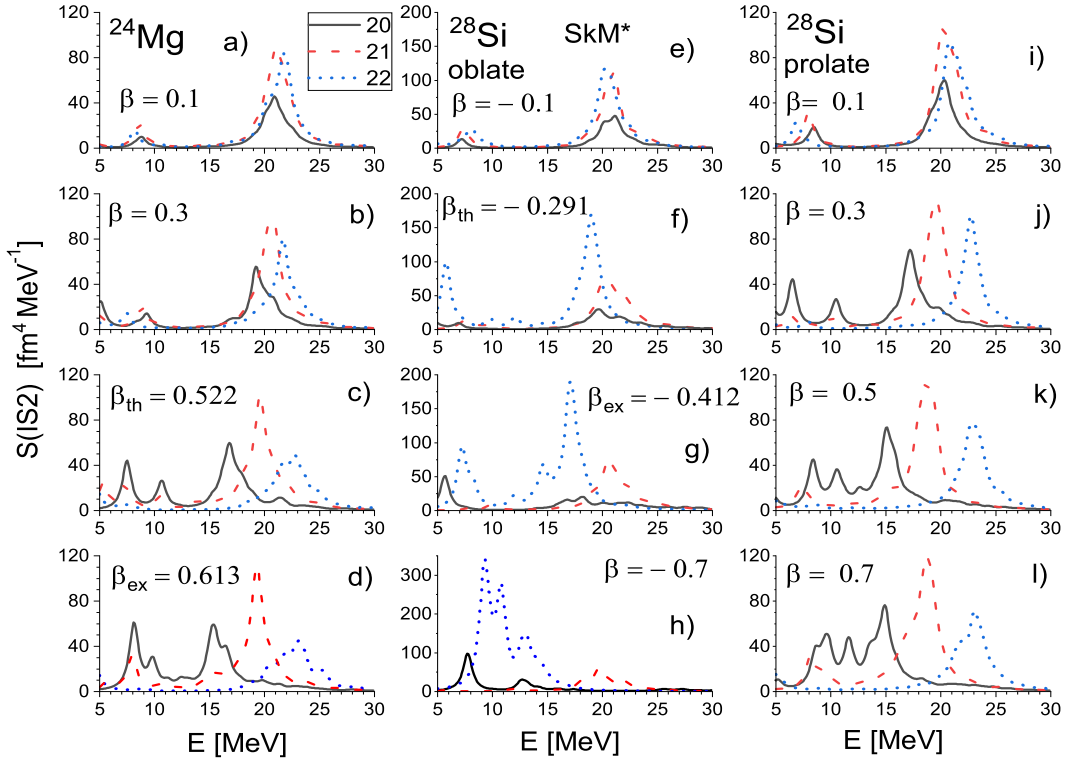


FIG. 14: ISGQR branches $LK = 20$ (solid black line), 21 (dashed red line) and 22 (dotted blue line) in ^{24}Mg and ^{28}Si , calculated with the force SkM* for different quadrupole deformations. For ^{28}Si , both oblate (middle panels) and prolate (right panels) deformations are considered.

TABLE X: EWSR exhaustion for the $LK = 20$, 21 and 22 branches of the ISGQR, calculated with the force SkM*.

	$^{24}\text{Mg}, \beta = 0.522$		$^{28}\text{Si}, \beta = -0.291$	
	($\text{fm}^4 \text{MeV}$)	(%)	($\text{fm}^4 \text{MeV}$)	(%)
20	4468	26.5	3650	17.5
21	7396	42.0	6998	33.7
22	5534	31.5	10144	48.8

incompressibility.

In the plots e)-h), the dependence of the ISGQR in ^{28}Si on an *oblate* quadrupole deformation is shown. The deformations are $\beta = -0.1$, -0.291 (calculated equilibrium values), -0.412 (experimental value) and -0.7 . In the oblate case, the deformation splitting demonstrates some surprising features. The $K = 0$ branch is not upshifted, as would be expected from analytic estimates [9], but downshifted from 21 MeV to ~ 13 MeV. The $K = 0$ strength is redistributed to a lower-energy region and significantly suppressed (see also Table X). The $K = 1$ branch keeps almost the same energy. The $K = 2$

branch is strongly downshifted from 21 MeV to 8 – 15 MeV and its strength is significantly enhanced (see also Table X). At the calculated ($\beta_{\text{th}} = -0.291$) and experimental ($\beta_{\text{ex}} = -0.412$) values of the quadrupole deformation, the $K = 0$ peak approaches the energy 17 – 18 MeV of the narrow monopole peak. So the force SkM* can in principle describe the narrow IS0 peak in ^{28}Si once we take a proper value of oblate quadrupole deformation.

In the plots i)-l), the dependence of ISGQR in ^{28}Si on a *prolate* quadrupole deformation is inspected. This case is interesting since some studies predict at 9 – 13 MeV in ^{28}Si superdeformed rotational bands based on prolate 0^+ band heads [22, 53–55]. As seen from Fig. 7, the total energy of ^{28}Si indeed has a local prolate minimum. The plots i)-l) show that the deformation splitting in prolate ^{28}Si would be rather similar to that in prolate ^{24}Mg . The $K = 0$ branch in prolate ^{28}Si indeed covers the relevant energy interval 8 – 16 MeV. Our calculations, therefore, do not contradict the suggestion [22, 53–55] that ^{28}Si can possess highly prolate states at excitation energies 9 – 13 MeV. Moreover, at $\beta = 0.3$, the $K = 0$ strength covers the energy interval 16 – 19 MeV where the experimental narrow IS0 peak is located. So, our SkM* calculations do not contradict that ^{28}Si , being oblate in the ground state, can have a prolate shape for 0^+ excitations.

Altogether, the present analysis allows for the conclusion that the description of the experimental narrow IS0 peaks: i) in the case of ^{24}Mg , needs a Skyrme force like

SkP $^\delta$ ($K_\infty = 202$ MeV) with a low nuclear incompressibility and ii) in the case of ^{28}Si , can be achieved with

both SkP $^\delta$ and SkM* ($K_\infty = 217$ MeV) forces once we allow for oblate and prolate quadrupole deformation.

-
- [1] J. Blaizot, Phys. Rep. **64**, 171 (1980).
- [2] M. N. Harakeh and A. van der Woude, *Giant Resonances: Fundamental High-Frequency Modes of Nuclear Excitation* Oxford Studies in Nuclear Physics Vol. 24 (Oxford University Press, New York, 2001).
- [3] U. Garg and G. Colò, Prog. Part. Nucl. Phys. **101**, 55 (2018).
- [4] Y. Abgrall, B. Morand, E. Caurier, and N. Grammaticos, Nucl. Phys. A **346**, 431 (1980).
- [5] S. Jang, Nucl. Phys. A **401**, 303 (1983).
- [6] S. Nishizaki and K. Ando, Prog. Theor. Phys. **73**, 889 (1985).
- [7] M. Buenerd, D. Lebrun, P. Martin, P. de Saintignon, and C. Perrin, Phys. Rev. Lett. **45**, 1667 (1980).
- [8] U. Garg, P. Bogucki, J. D. Bronson, Y. W. Lui, and D. H. Youngblood, Phys. Rev. C **29**, 93 (1984).
- [9] J. Kvasil, V. O. Nesterenko, A. Repko, W. Kleinig, and P.-G. Reinhard, Phys. Rev. C **94**, 064302 (2016).
- [10] G. Colò, D. Gambacurta, W. Kleinig, J. Kvasil, V. O. Nesterenko, and A. Pastore, Phys. Lett. B **811**, 135940 (2020).
- [11] A. Bohr and B. R. Mottelson, *Nuclear Structure, Vol. II* World Scientific, Singapore, (1998).
- [12] Y. K. Gupta, U. Garg, J. T. Matta, D. Patel, T. Peach, J. Hoffman, K. Yoshida, M. Itoh, M. Fujiwara, K. Hara, H. Hashimoto, K. Nakanishi, M. Yosoi, H. Sakaguchi, S. Terashima, S. Kishi, T. Murakami, M. Uchida, Y. Yasuda, H. Akimune, T. Kawabata, and M. N. Harakeh, Phys. Lett. B **748**, 343 (2015).
- [13] J. Kvasil, V. O. Nesterenko, A. Repko, P.-G. Reinhard, and W. Kleinig, EPJ Web of Conferences **107**, 05003 (2016).
- [14] Y. K. Gupta, U. Garg, J. Hoffman, J. T. Matta, P. V. Madhusudhana Rao, D. Patel, T. Peach, K. Yoshida, M. Itoh, M. Fujiwara, K. Hara, H. Hashimoto, K. Nakanishi, M. Yosoi, H. Sakaguchi, S. Terashima, S. Kishi, T. Murakami, M. Uchida, Y. Yasuda, H. Akimune, T. Kawabata, and M. N. Harakeh, Phys. Rev. C **93**, 044324 (2016).
- [15] T. Kawabata, Few-Body Syst. **54**, 1457 (2013).
- [16] T. Peach, U. Garg, Y. K. Gupta, J. Hoffman, J. T. Matta, D. Patel, P. V. Madhusudhana Rao, K. Yoshida, M. Itoh, M. Fujiwara, K. Hara, H. Hashimoto, K. Nakanishi, M. Yosoi, H. Sakaguchi, S. Terashima, S. Kishi, T. Murakami, M. Uchida, Y. Yasuda, H. Akimune, T. Kawabata, M. N. Harakeh, and G. Colò, Phys. Rev. C **93**, 064325 (2016).
- [17] J. C. Zamora, C. Sullivan, R. G. T. Zegers, N. Aoi, L. Batail, D. Bazin, M. Carpenter, J. J. Carroll, Y. D. Fang, H. Fujita, U. Garg, G. Gey, C. J. Guess, M. N. Harakeh, T. H. Hoang, E. Hudson, N. Ichige, E. Ideguchi, A. Inoue, J. Isaak, C. Iwamoto, C. Kacir, N. Kobayashi, T. Koike, M. Kumar Raju, S. Lipschutz, M. Liu, P. von Neumann-Cosel, S. Noji, H.-J. Ong, S. Péru, J. Pereira, J. Schmitt, A. Tamii, R. Titus, V. Werner, Y. Yamamoto, X. Zhou, and S. Zhu, Phys. Rev. C **104**, 014607 (2021).
- [18] D. H. Youngblood, Y.-W. Lui, X.F. Chen, and H. L. Clark, Phys. Rev. C **80**, 064318 (2009).
- [19] D. H. Youngblood, Y.-W. Lui, and H. L. Clark, Phys. Rev. C **76**, 027304 (2007).
- [20] K. Yoshida, Modern Phys. Lett. A, **25**, 1783 (2010).
- [21] P. Adsley, V. O. Nesterenko, M. Kimura, L. M. Donaldson, R. Neveling, J. W. Brümmer, D. G. Jenkins, N. Y. Kheswa, J. Kvasil, K. C. W. Li, D. J. Marín-Lambarri, Z. Mabika, P. Papka, L. Pellegri, V. Pesudo, B. Rebeiro, P.-G. Reinhard, F. D. Smit, and W. Yahia-Cherif, Phys. Rev. C **103**, 044315 (2021).
- [22] P. Adsley, D. G. Jenkins, J. Cseh, S. S. Dimitrova, J. W. Brümmer, K. C. W. Li, D. J. Marín-Lambarri, K. Lukyanov, N. Y. Kheswa, R. Neveling, P. Papka, L. Pellegri, V. Pesudo, L. C. Pool, G. Riczu, F. D. Smit, J. J. van Zyl, and E. Zemlyanaya, Phys. Rev. C **95**, 024319 (2017).
- [23] R. Neveling, H. Fujita, F. D. Smit, T. Adachi, G. P. A. Berg, E. Z. Buthelezi, J. Carter, J. L. Conradie, M. Couder, R. W. Fearick, S. V. Förtsch, D. Fourie, Y. Fujita, J. Görres, K. Hatanaka, A. M. Heilmann, J. P. Mira, S. H. T. Murray, P. Von Neumann-Cosel, S. O'Brien, P. Papka, I. Poltoratska, A. Richter, E. Sideras-Haddad, J. A. Swartz, A. Tamii, I. T. Usman, and J. J. van Zyl, Nucl. Instrum. Methods Phys. Res., Sect. A **654**, 29 (2011).
- [24] A. Tamii, Y. Fujita, H. Matsubara, T. Adachi, J. Carter, M. Dozono, H. Fujita, K. Fujita, H. Hashimoto, K. Hatanaka, T. Itahashi, M. Itoh, T. Kawabata, K. Nakanishi, S. Ninomiya, A. B. Perez-Cerdan, L. Popescu, B. Rubio, T. Saito, H. Sakaguchi, Y. Sakemi, Y. Sasamoto, Y. Shimbara, Y. Shimizu, F. D. Smit, Y. Tameshige, M. Yosoi, and J. Zenhiro, Nucl. Instrum. Methods Phys. Res., Sect. A **605**, 326 (2009).
- [25] K. Van Der Borg, M. Harakeh, and A. Van Der Woude, Nucl. Phys. A **365**, 243 (1981).
- [26] Y. K. Gupta, K. B. Howard, U. Garg, J. T. Matta, M. Şenyigit, M. Itoh, S. Ando, T. Aoki, A. Uchiyama, S. Adachi, M. Fujiwara, C. Iwamoto, A. Tamii, H. Akimune, C. Kadono, Y. Matsuda, T. Nakahara, T. Furuno, T. Kawabata, M. Tsumura, M. N. Harakeh, and N. Kalantar-Nayestanaki, Phys. Rev. C **97**, 064323 (2018).
- [27] D. C. Patel, U. Garg, M. Itoh, H. Akimune, G. P. A. Berg, M. Fujiwara, M. N. Harakeh, C. Iwamoto, T. Kawabata, K. Kawase, J. T. Matta, T. Murakami, A. Okamoto, T. Sako, K. W. Schlax, F. Takahashi, M. White and M. Yosoi, Phys. Lett. B **735**, 387 (2014).
- [28] S. Brandenburg, R. De Leo, A. G. Drentje, M. N. Harakeh, H. Sakai and A. van der Woude, Phys. Lett. B **130**, 9 (1983).
- [29] G. R. Satchler and D. T. Khoa, Phys. Rev. C **55**, 285 (1997).
- [30] G. Fricke and C. Bernhardt, At. Data Nucl. Data Tables **60**, 177 (1995).
- [31] M. Rhoades-Brown, M. H. Macfarlane, and S. C. Pieper, Phys. Rev. C **21**, 2417 (1980).
- [32] M. Rhoades-Brown, M. H. Macfarlane, and S. C. Pieper, Phys. Rev. C **21**, 2436 (1980).
- [33] M. Nolte, H. Machner, and J. Bojowald, Phys. Rev. C

- 36**, 1312 (1987).
- [34] D. H. Youngblood, H. L. Clark, and Y.-W. Lui, *Phys. Rev. C* **60**, 014304 (1999).
- [35] D. H. Youngblood, H. L. Clark, and Y.-W. Lui, *Phys. Rev. C* **65**, 034302 (2002).
- [36] H. J. Lu, S. Brandenburg, R. De Leo, M. N. Harakeh, T. D. Poelheken, and A. van der Woude, *Phys. Rev. C* **33**, 1116 (1986).
- [37] H. Dennert, E. Aschenauer, W. Eyrich, A. Lehmann, M. Moosburger, N. Scholz, H. Wirth, H. J. Gils, H. Rebel, and S. Zagromski, *Phys. Rev. C* **52**, 3195 (1995).
- [38] National Nuclear Data Center (NNDC), Nuclear Science References (version of (2015)), information extracted from the NSR database <http://www.nndc.bnl.gov/ensdf/>
- [39] A. Repko, J. Kvasil, V. O. Nesterenko, P.-G. Reinhard, arxiv:1510.01248 (nucl-th), 2015.
- [40] A. Repko, J. Kvasil, V. O. Nesterenko, P.-G. Reinhard, *Eur. Phys. J. A* **53**, 221 (2017).
- [41] A. Repko, J. Kvasil, and V. O. Nesterenko, *Phys. Rev. C* **99**, 044307 (2019).
- [42] J. Kvasil, A. Repko, and V. O. Nesterenko, *Eur. Phys. J. A* **55**, 213 (2019).
- [43] M. Bender, P.-H. Heenen, and P.-G. Reinhard, *Rev. Mod. Phys.* **75**, 121 (2003).
- [44] J. R. Stone and P.-G. Reinhard, *Prog. Part. Nucl. Phys.* **58**, 587 (2007).
- [45] J. Bartel, P. Quentin, M. Brack, C. Guet, and H.-B. Håkansson, *Nucl. Phys. A* **386**, 79 (1982).
- [46] P. Klüpfel, P.-G. Reinhard, T. J. Bürvenich, and J. A. Maruhn, *Phys. Rev. C* **79**, 034310 (2009).
- [47] F. Tondeur, M. Brack, M. Farine, and J. M. Pearson, *Nucl. Phys. A* **420**, 297 (1984).
- [48] V. O. Nesterenko, W. Kleinig, J. Kvasil, P. Vesely, and P.-G. Reinhard, *Int. J. Mod. Phys. E* **17**, 89 (2008).
- [49] C. O. Kureba, Z. Buthelezi, J. Carter, G. R. J. Cooper, R. W. Fearick, S. V. Förtsch, M. Jingo, W. Kleinig, A. Krugmann, A. M. Krumbolz, J. Kvasil, J. Mabilia, J. P. Mira, V. O. Nesterenko, P. von Neumann-Cosel, R. Neveling, P. Papka, P.-G. Reinhard, A. Richter, E. Sideras-Haddad, F. D. Smit, G. F. Steyn, J. A. Swartz, A. Tamii, I. T. Usman, *Phys. Lett. B* **779**, 269 (2018).
- [50] J. Dobaczewski, W. Nazarewicz, and T. R. Werner, *Phys. Scripta T* **56**, 15 (1995).
- [51] P.-G. Reinhard, B. Schuettrumpf, and J. A. Maruhn, *Comp. Phys. Communic.* **258**, 107603 (2021).
- [52] V. O. Nesterenko, A. Repko, J. Kvasil, and P.-G. Reinhard, *Phys. Rev. Lett.* **120**, 182501 (2018).
- [53] Y. Taniguchi, Y. Kanada-En'yo, and M. Kimura, *Phys. Rev. C* **80**, 044316 (2009).
- [54] Y. Taniguchi and M. Kimura, *Phys. Lett. B* **800**, 135086 (2020).
- [55] A. V. Afanasjev and D. Ray *Journal of Physics: Conf. Series* **863**, 012052 (2017).
- [56] Y. Chiba and M. Kimura, *Phys. Rev. C* **91**, 061302(R) (2015).